



# Vibrational coherence in ultrafast electron-transfer dynamics of oxazine 1 in N,N-dimethylaniline: simulation of a femtosecond pump-probe experiment

B. Wolfseder <sup>a</sup>, L. Seidner <sup>b</sup>, W. Domcke <sup>b</sup>, G. Stock <sup>c</sup>, M. Seel <sup>d</sup>, S. Engleitner <sup>d</sup>,  
W. Zinth <sup>d</sup>

<sup>a</sup> *Institut für Physikalische and Theoretische Chemie, Technische Universität München, 85747 Garching, Germany*

<sup>b</sup> *Institut für Theoretische Chemie, Heinrich-Heine-Universität, 40225 Düsseldorf, Germany*

<sup>c</sup> *Fakultät für Physik, Universität Freiburg, 79104 Freiburg, Germany*

<sup>d</sup> *Institut für Medizinische Optik, Ludwig-Maximilians-Universität München, 80797 München, Germany*

Received 22 December 1997

## Abstract

Ultrafast intermolecular electron transfer in the oxazine/dimethylaniline system has been investigated with a time resolution of better than 20 fs. The time- and frequency-resolved differential transmission spectrum as well as the frequency-integrated pump-probe signal are reported. A detailed theoretical simulation of the spectroscopic data is performed, adopting a microscopic quantum mechanical model for the material system. The model includes electron-transfer coupling, intra-state electronic-vibrational coupling to two vibrational modes, as well as vibrational dissipation. The laser-matter interaction is included in a nonperturbative manner, thus fully including strong-field and pulse-overlap effects. The relationship between the electronic and vibrational relaxation dynamics of the molecular system and the structures observed in the transient spectra is discussed in detail. It is found that the population probability of the optically excited electronic state exhibits a biexponential decay characteristics. The rapid ( $\approx 50$  fs) initial decay is caused by the few vibrational modes strongly coupled to the ET reaction. The subsequent slower decay on a time scale of a few hundred femtoseconds reflects the vibrational cooling of the hot photoproducts. In particular, the simulations reproduce the coherent beating with a period of 55 fs observed in the experiment, which corresponds to an intramolecular vibrational mode that drives the ET process. © 1998 Elsevier Science B.V. All rights reserved.

## 1. Introduction

Thanks to the steady improvement of the time resolution in femtosecond laser spectroscopy, it is now possible to investigate in real time the dynamics of even the fastest electron-transfer (ET) processes. In recent experiments on intramolecular ET processes [1–4] as well as intermolecular ET processes

in solution [5–10] it has been found that the ET dynamics can be much faster than the solvation dynamics. It has been concluded that the ET process in such systems may be controlled by high-frequency intramolecular or intermolecular vibrational modes rather than the collective solvent response [4,6].

An interesting model system for the study of ultrafast ET is oxazine 1 ( $\text{OX1}^+$ ) in N,N-dimethyl-

aniline (DMA). Electron transfer occurs after optical excitation of  $\text{OX1}^+$  from the DMA molecule to the excited  $\text{OX1}^+$ . This type of process has been studied in detail by Yoshihara and collaborators using the fluorescence up-conversion technique [5–10]. The experiments indicate a lifetime of the excited state of  $\text{OX1}^+$  of less than 150 fs, limited by the time resolution of the experiment [8]. More recently, the ET dynamics in  $\text{OX1}^+$ /DMA has been investigated with considerably higher time resolution in a pump-probe (PP) experiment performed with laser pulses of  $\approx 15$  fs duration [11]. An ultrafast decay of the transmission has been observed which has been interpreted as an ET transfer process occurring on a 30–80 fs time scale [11]. In addition, pronounced oscillations reflecting coherent wave-packet motion on electronic ground-state and excited-state potential-energy surfaces have been observed [11]. Oscillatory features in femtosecond pump-probe spectra have been reported also for other ultrafast ET systems, e.g. tetracyanoethylene in pyrene [12] and tetracyanoethylene in  $\text{CCl}_4$  [13]. The oscillations have been interpreted in terms of vibrationally coherent ET dynamics [12,13].

The present paper reports additional experimental data for  $\text{OX1}^+$ /DMA, in particular, a two-dimensional time- and frequency-resolved differential transmission spectrum. The interpretation of these data in terms of ET dynamics and coherent vibrational dynamics is not straightforward, since several spectroscopic processes may contribute to the transmission signal. There are strong signatures of impulsive stimulated-Raman emission and of stimulated-emission from the excited electronic states, superimposed by weak excited-state absorption. Moreover, the ET reaction in  $\text{OX1}^+$ /DMA occurs on the same time scale as the duration of the laser pulses. As a consequence, pulse-overlap effects play a role on the short time scale of the ET process, thus hampering a simple and straightforward analysis of the signal.

To substantiate the interpretation of the experimental data, we have started a first attempt to simulate the time- and frequency-resolved transmission spectrum with a simple quantum-mechanical model. The simulation yields insight into the interplay of electronic and nuclear dynamics in ultrafast ET processes as well as into the relation between the material dynamics and the observed transient spectra.

## 2. Experimental section

The femtosecond pump-probe experiments were performed with an experimental system described in detail in Ref [11]. Here the most important features of the experimental set-up in brief: pump and probe pulses were generated by compressing amplified 50 fs pulses at 620 nm in two fibre-grating-prism combinations. The instrumental response function, i.e. the cross-correlation function of pump and probe pulses, had a width (FWHM) of less than 15 fs. Probe pulses were much weaker (by a factor of 20) than the pump pulses. The probe light transmitted through the sample (path length 100  $\mu\text{m}$ ) was analyzed by a monochromator-diode array combination [14]. In the figures the normalized transmission ( $\Delta T/T$ ) is plotted as a function of time delay and wavelength position. The sample consisted of oxazine 1 ( $\text{OX1}^+$ ) from Lambda, dissolved in dimethylaniline with weak traces ( $< 5\%$ ) of methanol at a concentration of  $4 \times 10^{-4}$  M.

For the simulation of the experimental data detailed information on the time dependence of the femtosecond light pulses is required. Since the pulse generation process used compression in a fibre-grating-prism system, we deduce the time-dependent intensity by simulating the compression process. In this way we obtained the intensity shown in Fig. 1a, solid line. This curve shows a width (FWHM) of the central part of the pulse of  $\approx 10$  fs, and some modulations in the wings. The shape is consistent with both the measured interferometric autocorrelation trace and the background-free cross-correlation function recorded when replacing the sample cell by a thin (50  $\mu\text{m}$ ) KDP crystal. The pulse generation process does not lead to bandwidth limited pulses since self-phase-modulation in the fibre produces a modulated spectrum (see Fig. 1b, solid curve). In the modelling procedure, the real pulse shape was simulated by a sum of two Gaussians: a long (36 fs) and weak (25% relative amplitude) pulse reproduced the wings, while a short pulse (6 fs) was used to account for the central part of the light pulses (dashed curve in Fig. 1a). It is evident from Fig. 1a that the central part of the simulating pulse is shorter than the experimental one. This short duration was introduced in order to reproduce qualitatively the large spectral width of the non-bandwidth limited (see above)

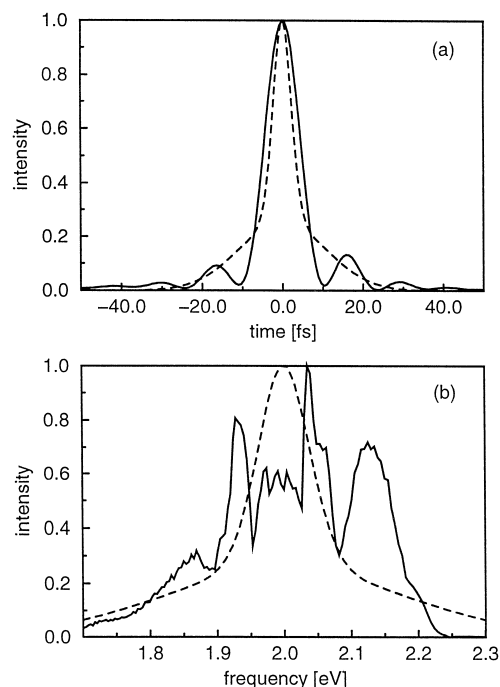


Fig. 1. (a) The estimated (see text) temporal intensity profile of a 10 fs Gaussian pulse with a carrier frequency of 2 eV (620 nm) after compression with a prism-compressor (full line) is compared to the intensity of the simulated pulse constructed as a superposition of Gaussian pulses of 6 fs and 36 fs duration (dashed line). (b) The spectrum of the experimental probe pulse (full line) is compared to the spectrum of the simulated pulse (dashed line).

probing pulses by the bandwidth limited modelling pulses (dashed curve in Fig. 1b). Otherwise numerical complications appeared when calculating the relative transmission changes in the wings of the spectrum.

### 3. Definition of the model

Starting from the available experimental data, our goal is to develop a “minimal” microscopic model of the photoinduced ET dynamics in  $\text{OX1}^+/\text{DMA}$ , that is, a model including the minimum number of electronic and vibrational degrees of freedom necessary to qualitatively reproduce the data observed. It has been found that this strategy leads to a model Hamiltonian that comprises three electronic states and two intramolecular vibrational modes. The large

number of remaining inter- and intramolecular vibrational modes of  $\text{OX1}^+/\text{DMA}$  are treated as a heat bath, which causes damping of the explicitly included modes (the so-called system modes). In contrast to previous models, where solvent effects have been simulated by a low-frequency classical solvent mode [4,6,15–17] or low-frequency quantum modes [18], we here adopt the reduced density-matrix approach, in which the bath degrees of freedom are traced out in a fully quantum mechanical manner [19–21]. Similar models have been considered, among others, by May, Schreiber and collaborators [22,23].

We consider three electronic states, the electronic ground state of the system ( $S_0$ ), the first excited singlet state ( $S_1$ ) of  $\text{OX1}^+$ , as well as the charge transfer (CT) state, which results from the transfer of an electron from DMA to the electronically excited  $\text{OX1}^+$ . It is assumed that the  $S_1$  state carries oscillator strength, while the CT state is dark in transitions to/from the electronic ground state. It is noted that conceptually similar models of the ET processes in  $\text{OX1}^+/\text{DMA}$  and related systems have previously been proposed by Yoshihara and collaborators [6,15].

In order to specify the vibrational degrees of freedom which are relevant for the ET dynamics in  $\text{OX1}^+/\text{DMA}$ , the CW absorption and the resonance-Raman spectra of the system have been analyzed [24]. Since the electronic dephasing defining the time window accessible by the CW spectra and the ET process occurs on the same time scale, it may be expected that the vibrational modes dominating the CW spectra are also important for the ET. The resonance-Raman spectrum of  $\text{OX1}^+/\text{DMA}$  obtained with an excitation wavelength  $\lambda = 632.8$  nm exhibits two intense lines at a Stokes shift of  $\approx 600$   $\text{cm}^{-1}$  and several ( $\approx 7$ ) lines between  $\approx 1100$   $\text{cm}^{-1}$  and  $1400$   $\text{cm}^{-1}$  [24]. Since these general features have also been found in resonance-Raman spectra of  $\text{OX1}^+$  on a graphite surface [25], it is concluded that these excitations correspond to intramolecular vibrational modes. This finding suggests that at least one high-frequency mode (henceforth denoted by  $\nu_1$ ) and one low-frequency mode ( $\nu_2$ ) is necessary to roughly describe the Condon activity of the system. The frequency of the low-frequency mode  $\nu_2$  is easily determined from the resonance-Raman spectrum as  $\omega_2 = 0.075$  eV ( $605$   $\text{cm}^{-1}$ ). Restricting ourselves to

a single high-frequency mode, the frequency  $\omega_1 = 0.17$  eV ( $1371$  cm $^{-1}$ ) of this “effective” mode is fixed by the requirement that the thus obtained model reproduces the high-frequency shoulder of the CW absorption spectrum (see below).

Guided by these considerations, the Hamiltonian of the system (defined by the three electronic states and the two relevant vibrational modes) is written as

$$H_S = \sum_{i=0,1,CT} |\varphi_i\rangle h_i \langle \varphi_i| + \{|\varphi_{CT}\rangle g \langle \varphi_1| + \text{h.c.}\}, \quad (3.1)$$

where the  $|\varphi_i\rangle$  are diabatic electronic states representing the  $S_0$  state, the CT state, and the  $S_1$  state of the  $\text{OX1}^+/\text{DMA}$  complex, respectively. The parameter  $g$ , which is taken as constant (i.e., independent of the nuclear coordinates), represents the ET coupling. The vibrational Hamiltonians  $h_i$  are described in the harmonic approximation, whereby equal vibrational frequencies  $\omega_1, \omega_2$  are assumed in all three electronic states. The equilibrium geometries of the excited states, on the other hand, are shifted with respect to the ground state.

Introducing the usual annihilation and creation operators  $b_m^{(0)}, b_m^{(0)\dagger}$  ( $m=1,2$ ) of the harmonic oscillators in the electronic ground state, the corresponding operators for the excited states are given by

$$b_m^{(i)} = b_m^{(0)} + \frac{\kappa_m^{(i)}}{\sqrt{2} \omega_m}, \quad (3.2)$$

where  $\kappa_m^{(i)}$  is the electron-vibrational coupling parameter of the  $m$ th mode in the electronic state  $|\varphi_i\rangle$ . In terms of these operators, the vibrational Hamiltonians read ( $\hbar = 1$ )

$$h_i = \begin{cases} \sum_{m=1,2} \omega_m (b_m^{(0)\dagger} b_m^{(0)} + \frac{1}{2}) \\ (i=0) \\ \bar{E}_i + \sum_{m=1,2} \omega_m (b_m^{(i)\dagger} b_m^{(i)} + \frac{1}{2}) \\ (i=1,CT). \end{cases} \quad (3.3)$$

The  $\bar{E}_i$  are the excitation energies for the vibrational 0–0 transition; they are related to the vertical electronic excitation energies via  $\bar{E}_i = E_i - \sum_m \kappa_m^{(i)2} / (2 \omega_m)$ .

To describe the coupling of the molecular system

$H_S$  with the laser fields, we furthermore introduce the radiation–matter interaction  $H_{\text{int}}(t)$ , which in the dipole approximation is given as

$$H_{\text{int}}(t) = -|\varphi_1\rangle \boldsymbol{\mu}_{01} \cdot \mathbf{E}(t) \langle \varphi_0| + \text{h.c.} \quad (3.4)$$

Here  $\boldsymbol{\mu}_{01}$  is the transition dipole moment of the allowed electronic transition ( $S_0 \rightarrow S_1$ ), which is assumed to be independent of the vibrational coordinates (Condon approximation). The electric field  $\mathbf{E}(t)$  consists of the pump field  $\mathbf{E}_1(t)$  and the probe field  $\mathbf{E}_2(t)$  with wave vectors  $\mathbf{k}_1$  and  $\mathbf{k}_2$ , respectively

$$\mathbf{E}(\mathbf{x}, t) = \mathbf{E}_1(t) e^{i\mathbf{k}_1 \cdot \mathbf{x}} + \mathbf{E}_2(t) e^{i\mathbf{k}_2 \cdot \mathbf{x}} + \text{c.c.}, \quad (3.5)$$

$$\mathbf{E}_i(t) = \boldsymbol{\epsilon}_i \mathcal{E}_i(t) e^{-i\omega_i t}, \quad (3.6)$$

where  $\mathcal{E}_i(t)$  denotes the pulse envelope function,  $\boldsymbol{\epsilon}_i$  the polarization vector, and  $\omega_i$  the carrier frequency of the  $i$ th pulse.

Assuming bilinear coupling between the system modes and the bath modes, the latter can approximately be integrated out, as is described in detail elsewhere [21,26,27]. This derivation invokes the usual Born and Markov approximations as well as the assumption that the bath remains in thermal equilibrium [19,20]. Moreover, the effect of the ET coupling and the matter–field coupling on dissipation is neglected.

The resulting equation of motion for the reduced density operator  $\rho(t)$ , defined as the trace of the density operator over the bath variables, reads

$$\frac{\partial}{\partial t} \rho(t) = -i [H_S + H_{\text{int}}(t), \rho(t)] + L(\rho). \quad (3.7)$$

Employing the rotating-wave approximation for the system–bath coupling, the relaxation operator is given by [21]

$$\mathcal{L}(\rho) = \frac{1}{2} \sum_{i,j=0,1,2} |\varphi_i\rangle \lambda^{(ij)} \langle \varphi_j| \quad (3.8)$$

with

$$\begin{aligned} \lambda^{(ij)} = & \sum_{m=1,2} (\langle n_m \rangle + 1) (2C_m^{(i)} \rho^{(ij)} C_m^{(j)\dagger} \\ & - C_m^{(i)\dagger} C_m^{(i)} \rho^{(ij)} - \rho^{(ij)} C_m^{(j)\dagger} C_m^{(j)}) \\ & + \langle n_m \rangle (2C_m^{(i)\dagger} \rho^{(ij)} C_m^{(j)} - C_m^{(i)} C_m^{(i)\dagger} \rho^{(ij)} \\ & - \rho^{(ij)} C_m^{(j)} C_m^{(j)\dagger}), \end{aligned} \quad (3.9)$$

where we have introduced the electronic matrix elements of the reduced density operator  $\rho^{(ij)} = \langle \varphi_i | \rho | \varphi_j \rangle$  and the definition  $C_m^{(i)} = \sqrt{\Gamma_m^{(i)}} b_m^{(i)}$ . Furthermore,  $\Gamma_m^{(i)}$  denotes the relaxation rate of the  $m$ th vibrational mode in electronic state  $|\varphi_i\rangle$ , and  $\langle n_m \rangle = [e^{\omega_m/k_B T} - 1]^{-1}$  is the thermal occupation distribution. Since temperature effects are not important for the ET reaction considered here, the temperature  $T$  is set to zero throughout this work.

The values of the parameters specifying the model for the material system are collected in Table 1. As explained above, the frequencies of the two intramolecular vibrational modes  $\omega_1 = 0.17$  eV (1371  $\text{cm}^{-1}$ ) and  $\omega_2 = 0.075$  eV (605  $\text{cm}^{-1}$ ) have been deduced from the analysis of the CW absorption and resonance-Raman spectra of  $\text{OX1}^+/\text{DMA}$ . The high-frequency mode  $\nu_1$  represents an effective vibrational mode that accounts for the superposition of several intramolecular modes of similar frequencies. It may be expected that the dynamics of such a cluster of modes will exhibit a rapid dephasing process. We have accounted for this effect by adopting a large damping parameter  $\Gamma_1$  for the high-frequency mode  $\nu_1$ . The damping parameter  $\Gamma_2$  of the low-frequency mode  $\nu_2$  has been adjusted to reproduce the vibrational dephasing of the coherent 55 fs oscillations observed in the PP signal. For both modes we assume stronger damping in the excited states than in the ground state (see Table 1).

The parameters characterizing the potential-energy surface of the optically bright state have been obtained from the simulation of the CW absorption spectrum of  $\text{OX1}^+/\text{DMA}$  with the present model. From this calculation the vertical excitation energy of the  $S_1$  state ( $E_1 = 2.0$  eV) and the electron-vibrational coupling constants  $\kappa_1^{(1)}$ ,  $\kappa_2^{(1)}$  of the  $S_1$  state

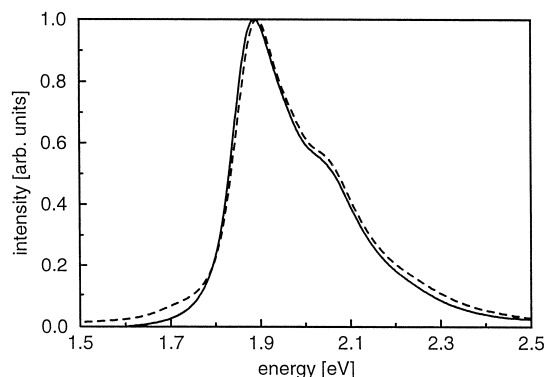


Fig. 2. The experimental CW absorption spectrum of  $\text{OX1}^+$  in DMA (full line) is compared to the simulated spectrum (dashed line). The peak of the CW-absorption is at 1.9 eV, corresponding to 657 nm.

have been deduced. Furthermore, an optical dephasing parameter,  $T_2 = 40$  fs, has been included in the calculation of the CW absorption spectrum. Fig. 2 compares the simulated spectrum (dashed line) to the experimental result (full line). Despite of the certainly oversimplified model employed, the simulation is in very good agreement with the experiment.

It remains to determine the parameters of the potential-energy surface ( $E_{\text{CT}}$ ,  $\kappa_1^{(\text{CT})}$ ,  $\kappa_2^{(\text{CT})}$ ) of the dark CT state and the ET coupling  $g$ . In the absence of relaxation effects caused by the vibrational degrees of freedom, the electronic population of the system would oscillate between the initially excited electronic state  $|\varphi_1\rangle$  and the CT state  $|\varphi_{\text{CT}}\rangle$ . The frequency of these Rabi oscillations solely depends on the interstate coupling constant  $g$  and the energy gap  $E_1 - E_{\text{CT}}$  between the two electronic states. To reproduce the rapid initial decay observed in the time-resolved experiments, the coupling constant  $g$

Table 1

Parameters of the  $\text{OX1}^+/\text{DMA}$  model

$E_0$	$E_{\text{CT}}$	$E_1$	$g$	
0	1.744 eV (14066 $\text{cm}^{-1}$ )	2.0 eV (16131 $\text{cm}^{-1}$ )	0.03 eV (242 $\text{cm}^{-1}$ )	
$\omega$	$\kappa^{(\text{CT})}$	$\kappa^{(1)}$	$\Gamma^{(0)}$	$\Gamma^{(\text{CT})} = \Gamma^{(1)}$
0.17 eV (1371 $\text{cm}^{-1}$ )	−0.05 eV (−403 $\text{cm}^{-1}$ )	0.17 eV (1371 $\text{cm}^{-1}$ )	0.03 eV (242 $\text{cm}^{-1}$ )	0.05 eV (403 $\text{cm}^{-1}$ )
0.075 eV (605 $\text{cm}^{-1}$ )	−0.06 eV (−484 $\text{cm}^{-1}$ )	0.067 eV (540 $\text{cm}^{-1}$ )	0.003 eV (24 $\text{cm}^{-1}$ )	0.005 eV (40 $\text{cm}^{-1}$ )

is chosen as 0.03 eV corresponding to a period of 138 fs of the Rabi oscillations. A stronger vibronic coupling strength leads to a contribution in the low-energy part of the CW absorption spectrum representing levels of the CT state which have borrowed intensity from the allowed  $S_1$  state by vibronic coupling. The absence of this contribution in the experimental CW spectrum points to a weak interstate coupling constant. Furthermore, to ensure an ultra-fast electronic decay, the electronic energy gap has to be chosen such that the intersection of the two diabatic excited electronic potentials lies below the vertical excitation energy  $E_1$ . Yoshihara and coworkers postulated that the ET reaction is activationless with an energy gap  $E_1 - E_{CT}$  of 0.496 eV [28]. With this choice of parameters the initial decay would take place on a timescale which is much slower than the experimental results of Zinth and coworkers demonstrate [11]. To obtain a faster ET reaction, we choose appropriately modified parameters for the CT state (Table 1). Since the  $S_1$  potential-energy surface obtained by the fitting of the CW absorption spectrum exhibits only a relatively small coordinate shift, the vertical excitation energy lies close to the minimum of the  $S_1$  state (see Fig. 3). As a consequence, the possible values for the electron-vibrational coupling constants  $\kappa_1^{(CT)}$ ,  $\kappa_2^{(CT)}$  are strongly limited. In consideration of these restrictions, the intrastate coupling constants and the vertical excitation energy  $E_{CT}$  have independently been varied to optimize the agreement of the calculated time-resolved PP signal with the experimental data. Since this fitting procedure is not necessarily unique, we cannot claim to have found the best possible model within the theoretical framework defined by Eqs. (3.1), (3.7), (3.8) and (3.9).

Let us finally turn to the description of the laser fields employed in the simulation. As in the experiment, the laser carrier frequency used in the calculations is 2.0 eV, i.e., the laser is resonant with the vertical  $S_0$ – $S_1$  transition. The transition dipole moment and the intensity of the pump pulse are chosen such that  $\approx 12\%$  of the electronic population are transferred to the  $S_1$  state, as estimated in the experiment. The intensity of the probe pulse is smaller than the intensity of the pump pulse by a factor of 16. To simplify the calculations, the temporal intensity profile of the laser pulses has been approximated by a superposition of two Gaussian functions with a

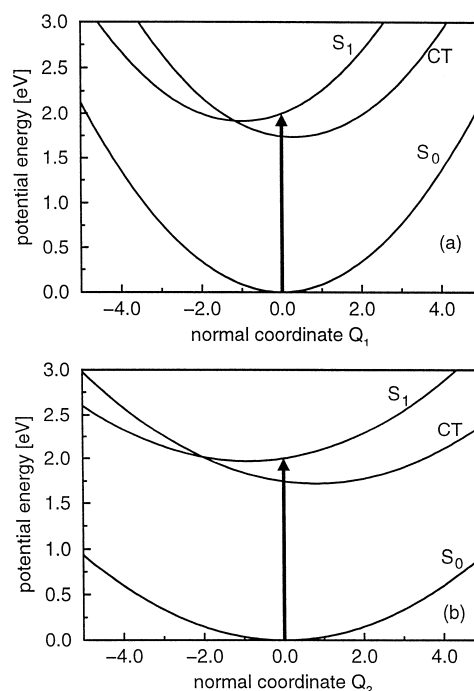


Fig. 3. Diabatic potential-energy functions of the vibrational mode  $\nu_1$  (a) and the vibrational mode  $\nu_2$  (b). The arrow indicates vertical excitation from the ground state.

halfwidth (fwhm) of 6 fs and 36 fs. The pulse envelope used in the calculations is compared with the experimentally estimated temporal intensity profile in Fig. 1. Test calculations have shown that the basic properties of the signals considered here are not particularly sensitive to the detailed shape of the pump and probe pulses.

## 4. Computational methods

### 4.1. Propagation of the reduced density matrix

The equation of motion (3.7) for the reduced density matrix is solved numerically, thus treating the intra-system dynamics as well as the driving of the system by the laser field in a nonperturbative manner. To this end, the Hamiltonians  $H_S$ ,  $H_{int}(t)$  and the reduced density operator are represented in a direct-product basis constructed from the three elec-

tronic states and harmonic-oscillator basis states for each of the two vibrational modes. Converged results are obtained with maximum occupation numbers  $v_1^{\max} = 12$  and  $v_2^{\max} = 14$ . The dimension of the Hilbert space of the system is thus  $N = 585$ , and the reduced density matrix at a given time  $t$  is specified by a vector of dimension  $N(N+1)/2 = 171405$ .

The standard and most straightforward way to proceed is to directly solve the thus obtained set of  $N(N+1)/2$  coupled first-order differential equations. Computations of this type for systems with two vibrational degrees of freedom have been reported, for example, in Refs. [29,30]. In the present work we have adopted an alternative approach, the Monte Carlo wave-function (MCWF) method, which has the advantage of being applicable also for larger systems, e.g., models involving three or four strongly coupled vibrational modes. This is so because the computational cost of the MCWF method increases only linearly with  $N$ , while the cost of the conventional numerical approach scales as  $N^2$ .

In the MCWF method, which has been developed in the context of quantum optical applications, the propagation of the density matrix is replaced by an ensemble of wave-function propagations [31–34]. The application of the MCWF method to few-state few-mode vibronic-coupling and electron-transfer problems has been described recently [27,35], and we refer to these articles for details.

In the present application we have applied the MCWF method to evaluate directionally resolved nonlinear polarizations. It turned out that the first-order accuracy of the MCWF method as described in Refs. [31–34] is not sufficient for this purpose. As discussed in Ref. [36], higher accuracy and a more rapid convergence of the Monte Carlo scheme can be achieved with higher-order implementations of the MCWF method. A second-order scheme has been found appropriate for the present purposes [37,38]. Reasonably converged results are obtained with 1000 realizations of the stochastic process.

Once the reduced density matrix has been calculated, all observables of interest can readily be obtained. Let us introduce several time-dependent observables of the molecular system, which have proven to be of importance in the interpretation of electronic and vibrational relaxation processes [40]. A key quantity for the description of ET dynamics is the

time-dependent population probability of the electronic state  $|\varphi_1\rangle$  after preparation by the pump pulse, defined as

$$W_1(t) = \text{Tr} \{ \rho^{(11)}(t) \}, \quad (4.1)$$

where the trace is taken over the vibrational states. To monitor the coherence of vibrational motion, we consider the expectation values of the position and momentum operators

$$\langle Q_m \rangle_t = \text{Tr} \{ Q_m \rho(t) \}, \quad \langle P_m \rangle_t = \text{Tr} \{ P_m \rho(t) \}, \quad (4.2)$$

where  $Q_m$  is the normal coordinate and  $P_m$  the momentum of the  $m$ th vibrational mode.

#### 4.2. Calculation of the spectroscopic signal

The signal measured in the present experiment is the differential probe-transmission spectrum, defined as [39,40]

$$\begin{aligned} I_{\text{TS}}(\omega, \Delta t) &= \frac{I^{\text{pump on}}(\omega, \Delta t) - I^{\text{pump off}}(\omega)}{I^{\text{pump off}}(\omega)} \\ &= 2\omega \text{Im} \frac{\tilde{P}_{k_2}^*(\omega)}{E_2(\omega)}. \end{aligned} \quad (4.3)$$

Here  $\tilde{P}_{k_2}(\omega) = P_{k_2}^{\text{pump on}} - P_{k_2}^{\text{pump off}}$  is the Fourier transform of the transmission difference of the probe field (i.e., in the probe direction  $k_2$ ), with and without preparation of the medium by the pump pulse.  $E_2(\omega)$  denotes the Fourier transform of the probe field.

In the present work we have adopted the nonperturbative approach to the evaluation of the nonlinear polarization [41,42]. The polarization is directly determined from the density matrix of the laser-driven dissipative system

$$P(t) = \text{Tr} \{ \mu \rho(t) \} = 2\text{Re} \mu_{10} \text{Tr} \{ \rho^{(01)}(t) \}, \quad (4.4)$$

whereby the nonlinear part of the polarization is obtained in the usual way by taking the difference  $\tilde{P} = P^{\text{pump on}} - P^{\text{pump off}}$ . As described in detail in Ref. [41], the directional decomposition of the polarization is achieved by performing calculations for

four different relative phases of pump and probe fields. If  $P(\phi)$  denotes the polarization obtained with a given relative phase, the polarization propagating in  $k_2$  direction is given by [41]

$$P_{k_2} = \frac{1}{4} \{ P(0) + P(\pi/2) + P(\pi) + P(3\pi/2) \}, \quad (4.5)$$

where, for simplicity, the  $t$ -dependence has been suppressed.  $P(\omega)$  is obtained by a numerical fast Fourier transform.

## 5. Results and discussion

In Fig. 4 the experimental (a) and simulated (b) transient transmission spectra of  $\text{OX1}^+$  in DMA are displayed as a function of the probe transmission frequency and the time delay. Let us first briefly discuss the experimental spectrum. At negative delay times, where the probe pulse precedes the pump pulse, the spectrum exhibits a complicated pattern which is related to the coherent properties of the

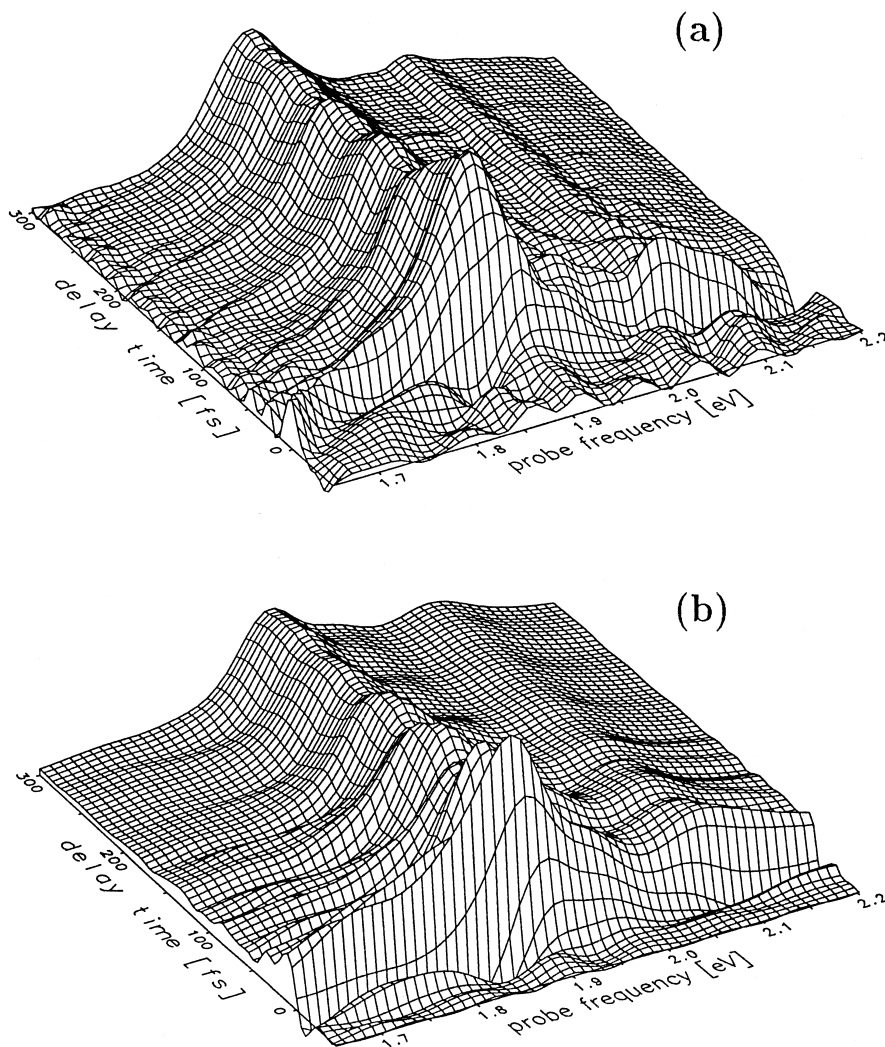


Fig. 4. The experimental transmission spectrum of  $\text{OX1}^+$  in DMA (a) is compared with the simulated transmission spectrum (b).



sample. Around time zero, when the two laser fields overlap in time, a coherent artifact occurs which hardly carries information on the material response. The rapid initial transmission increase at zero delay time is followed by an oscillatory rapid decay of the transmission which is completed after 150 fs. For larger delay times the PP signal is dominated by a slow decay with superimposed oscillations with a period of about 55 fs. A closer inspection shows a beating phenomenon pointing to the existence of two Raman active modes with frequencies of  $567\text{ cm}^{-1}$  and  $612\text{ cm}^{-1}$  [11]. These features are due to impulsive stimulated Raman excitation of ground state vibrational modes.

The theoretical simulation shown in Fig. 4(b) is seen to be in good overall agreement with the experimental signal. In particular, the calculation is able to reproduce qualitatively the interference structures at negative delay times, the overall appearance and decay of the emission bands, and the coherent oscillations of the signal. The limitations of our simple model become apparent, however, when considering specific cuts through the transmission spectrum. As a representative example, Fig. 5 shows the PP signal at the wavelengths 657 and 669 nm, which correspond to the maxima of the CW absorption and emission bands. Most noticeable, the onset and initial decay of the calculated transmission signals (Fig. 5b) is more rapid than observed in experiment (Fig. 5a). Apart from the thus introduced overall phase shift, the oscillatory features beyond 100 fs are well reproduced by the theoretical model. The discrepancy between the experimental and theoretical signals may be due to possible initial excited-state absorption to a higher-lying excited electronic state not included in the model, the restriction of the model to two vibrational modes, to uncertainties in the experimental determination of the zero delay-time, as well as to the too short laser pulses used in the simulation. Especially the rapid onset of the simulated signal will become slower if the duration of the laser pulses increases.

Let us turn to the discussion of the integral PP signal, which is obtained through integration of the dispersed transmission spectrum over all emission frequencies. As has been discussed in detail elsewhere [40,44,45], the integral PP signal gives for very short light pulses the most direct indication of

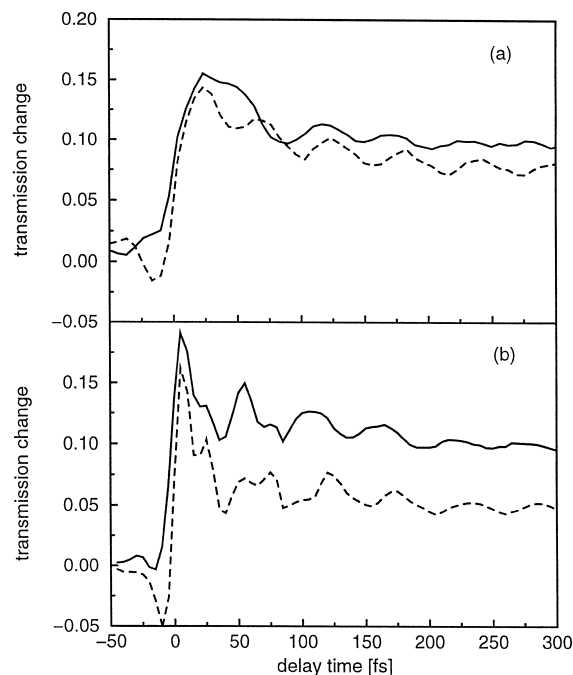


Fig. 5. Cuts through the transmission spectrum at the peak of the CW-absorption at 1.89 eV (657 nm) (full line) and the CW-emission at 1.85 eV (669 nm) (dashed line). (a) represents the experimental data and (b) the simulated results.

excited-state electronic population dynamics in a real-time experiment. This is because for an ultra-short probe pulse the integration over the emission frequencies “integrates out” the Condon oscillations of the signal due to the vibrational dynamics on a single potential-energy surface [44], thus solely displaying the electronic population dynamics of the system.

The experimental and calculated integral signals, normalized to the same peak value, are shown in Fig. 6. Similar to the dispersed PP signals shown in Fig. 5, the onset and initial decay of the integral signal is somewhat too fast in the simulation, thus introducing an overall phase shift. Most interestingly, both experimental and calculated signals clearly exhibit distinct coherent oscillations for larger delay times. The appearance of oscillations in the integral PP signal may be interpreted as a first indication that the oscillatory features of the signal do not only reflect vibrational motion on a single potential-energy surface, but could

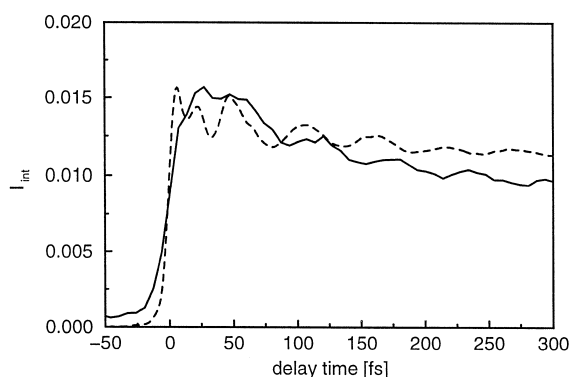


Fig. 6. Integral transmission spectrum with a probe carrier frequency of  $\omega_2 = 2$  eV (620 nm). The experimental signal (full line) is compared to the simulated results (dashed line).

directly be connected with the photoinduced ET process of the system. In fact, it has been found in a number of simulations of nonadiabatic relaxation dynamics in molecular systems that the coherent wave-packet motion drives the ET process, thus leading to coherent photoproducts [40].

However, the clear identification of the integral PP signal with the nonadiabatic electronic population dynamics is valid only for the idealized situation of an ultrashort laser pulse, in which case the pump and probe pulses do not overlap and the stimulated-emission contribution clearly dominates the signal. The conditions here are more involved since the ET process in OX1<sup>+</sup>/DMA occurs on the same time scale as the duration of the laser pulses. As a consequence, pulse-overlap effects have to be taken into account in the analysis of the signal and the signal cannot simply be interpreted in terms of the stimulated-emission and the stimulated-Raman contributions, which separately reflect the excited-state and the ground-state dynamics, respectively [40,43].

On the other hand, the theoretical simulation allows us to interpret the spectroscopic signatures in terms of the features of the underlying material dynamics, that is, the ET process and the vibrational dynamics. It is instructive to compare the simulated integral PP signal shown in Fig. 6 to the time-dependent population probability of the optically prepared electronic state shown in Fig. 7. Although for reasons explained above the initial features of the two observables are somewhat different, it is seen that the electronic population probability also exhibits

oscillations. This finding supports the idea that the oscillations of the PP signal may reflect coherently driven ET dynamics.

It is noted that the population probability of the  $S_1$  state exhibits a biexponential decay characteristics which consists of a fast initial decay on a time scale of about 50 fs and a slower decay on a time scale of a few hundred femtoseconds. As has been discussed in Ref. [35], the rapid initial decay is governed by the system Hamiltonian and is largely independent of the dissipation, while the slower decay reflects the vibrational cooling of the vibrationally hot photoproduct in the CT state.

Apart from the electronic dynamics discussed so far, it is also interesting to see to what extent the vibrational dynamics of the system is reflected in the PP signals. With this end in mind, let us consider the expectation values of position and momentum of both vibrational modes displayed in Fig. 8. As may be expected from the relatively strong vibrational relaxation parameters adopted by our model, the high-frequency mode  $\nu_1$  is strongly damped and relaxes to equilibrium within  $\approx 100$  fs. The coherent oscillations of the 55 fs mode, on the other hand, are seen to survive for a few hundred femtoseconds. It is instructive to compare the vibrational dynamics displayed in Fig. 8 to the recurrences observed in the simulated integral PP spectrum in Fig. 6. The oscillation of the signal, with pronounced maxima at 55 fs, 110 fs, and 165 fs obviously mirrors the coherent vibrational motion in the 55 fs mode, which is driven

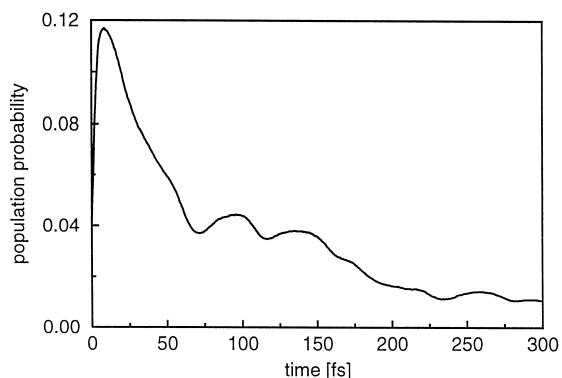


Fig. 7. Time-dependent population probability of the optically bright electronic state  $|\varphi_1\rangle$  prepared with the pump pulse of the present simulation.

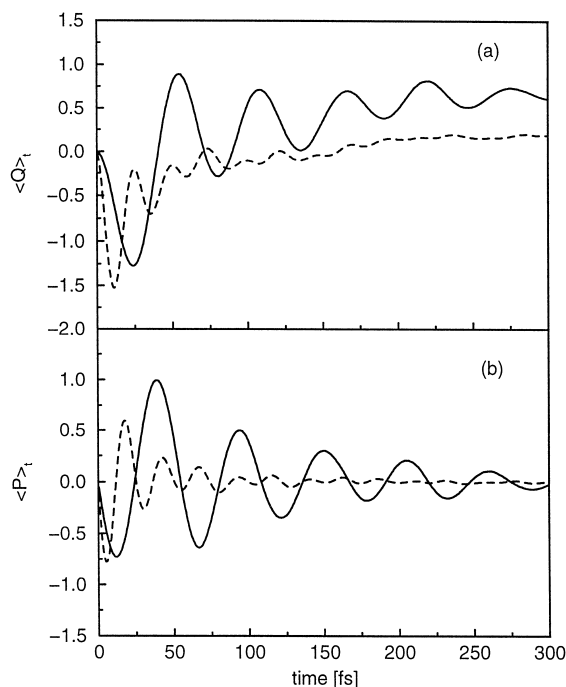


Fig. 8. Time evolution of the expectation values of (a) position and (b) momentum for the vibrational mode  $\nu_1$  with frequency  $\omega_1 = 0.17$  eV (dashed line) and for the normal mode  $\nu_2$  with frequency  $\omega_2 = 0.075$  eV (full line).

by the gradient of the potential-energy surface of the  $S_1$  state. The maxima of the PP signal (Fig. 6) are seen to correlate with the inner turning points of this mode, see Fig. 8a. The weak oscillations of the signal at longer times reflect coherent vibrational motion in the electronic ground state, for which only a weak vibrational damping has been assumed.

## 6. Conclusions

We have described an attempt towards the development of a complete theoretical simulation of the time and frequency resolved PP spectrum for the ultrafast ET system  $\text{OX1}^+/\text{DMA}$ . The model for the material dynamics is based on the assumption of three relevant electronic states and two strongly coupled fast vibrational modes. The remaining degrees of freedom have been treated as a dissipative environment. The ET coupling, the intra-state electron-vibrational couplings as well as the field-matter

interaction have been treated nonperturbatively via a numerical solution of the equation of motion of the density matrix. Commonly employed approximations such as the assumption of weak laser pulses,  $\delta$ -function pulses, or ultrafast optical dephasing have been avoided. In particular, resonant pulse-overlap effects (the coherent artifact) are fully included in the present simulation.

Although a quantitative agreement between the theoretical simulation and the experiment was not obtained, the calculations have provided useful qualitative insight into the dynamics of the ultrafast ET process. The model calculations have revealed the interplay of ET dynamics and coherent and dissipative vibrational dynamics and how these phenomena are reflected in the time and frequency resolved PP spectrum. To arrive at a quantitative understanding of the dynamics of this interesting ET system, however, a better characterization and a more realistic modeling of the laser pulses and the system dynamics is necessary. *Ab initio* electronic-structure calculations should be feasible for this system. They should provide information on the number of electronic and vibrational states actively involved in the ET reaction and on the shape of the potential-energy surfaces.

## Acknowledgements

This work has been supported by the Deutsche Forschungsgemeinschaft and the Fonds der Chemischen Industrie. We thank A. Lau for providing us with resonance Raman spectra of oxazine on graphite.

## References

- [1] E. Åkesson, G.C. Walker, P.F. Barbara, J. Chem. Phys. 95 (1991) 4188.
- [2] E. Åkesson, A.E. Johnson, N.E. Levinger, G.C. Walker, T.P. DuBrail, P.F. Barbara, J. Chem. Phys. 96 (1992) 7859.
- [3] P.J. Reid, C. Silva, P.F. Barbara, L. Karki, J.T. Hupp, J. Phys. Chem. 99 (1995) 2609.
- [4] G.C. Walker, E. Åkesson, A.E. Johnson, N.E. Levinger, P.F. Barbara, J. Phys. Chem. 96 (1992) 3728.
- [5] Y. Nagasawa, A.P. Yartsev, K. Tominaga, P.B. Bisht, A.E. Johnson, K. Yoshihara, J. Phys. Chem. 99 (1995) 653.
- [6] K. Yoshihara, K. Tominaga, Y. Nagasawa, Bull. Chem. Soc. Japan 68 (1995) 696.

- [7] T. Kobayashi, Y. Takagi, H. Kandori, K. Kemnitz, K. Yoshihara, *Chem. Phys. Lett.* 180 (1991) 416.
- [8] A. Yartsev, Y. Nagasawa, A. Douhal, K. Yoshihara, *Chem. Phys. Lett.* 207 (1993) 416.
- [9] H. Kandori, K. Kemnitz, K. Yoshihara, *J. Phys. Chem.* 96 (1992) 8042.
- [10] K. Kemnitz, K. Yoshihara, *Chem. Lett.* 1991 (1991) 645.
- [11] M. Seel, S. Engleitner, W. Zinth, *Chem. Phys. Lett.* 275 (1997) 363.
- [12] K. Wynne, G.D. Reid, R.M. Hochstrasser, *J. Chem. Phys.* 105 (1996) 2287.
- [13] I.V. Rubtsov, K. Yoshihara, *J. Chem. Phys. A* 101 (1997) 6138.
- [14] M. Seel, E. Wildermuth, W. Zinth, *Meas. Sci. Technol.* 8 (1997) 449.
- [15] K. Yoshihara, H. Pal, H. Shirota, Y. Nagasawa, K. Tominaga, in: M. Chergui (Ed.), *Femtochemistry*, World Scientific, Singapore, 1996.
- [16] H. Sumi, R.A. Marcus, *J. Chem. Phys.* 84 (1986) 4894.
- [17] J. Jortner, M. Bixon, *J. Chem. Phys.* 88 (1988) 167.
- [18] M. Bixon, J. Jortner, *J. Chem. Phys.* 107 (1997) 1470.
- [19] A.G. Redfield, *Advan. Magn. Reson.* 1 (1965) 1.
- [20] K. Blum, *Density matrix theory and applications*, Plenum, New York, 1981.
- [21] T. Takagahara, E. Hanamura, R. Kubo, *J. Phys. Soc. Japan* 44 (1978) 728.
- [22] C. Fuchs, M. Schreiber, *J. Chem. Phys.* 105 (1996) 1023.
- [23] O. Kühn, T. Renger, V. May, *Chem. Phys.* 204 (1996) 99.
- [24] I. Hartl, W. Zinth, unpublished results.
- [25] A. Lau, personal communication.
- [26] V. May, M. Schreiber, *Phys. Rev. A* 45 (1992) 2868.
- [27] B. Wolfseder, W. Domcke, *Chem. Phys. Lett.* 235 (1995) 370.
- [28] Y. Nagasawa, A.P. Yartsev, K. Tominaga, A.E. Johnson, K. Yoshihara, *J. Chem. Phys.* 101 (1994) 5717.
- [29] O. Kühn, T. Renger, V. May, *Chem. Phys.* 204 (1996) 99.
- [30] L. Pesce, P. Saalfrank, *Chem. Phys.* 219 (1997) 43.
- [31] J. Dalibard, Y. Castin, K. Mølmer, *Phys. Rev. Lett.* 68 (1992) 580.
- [32] R. Dum, P. Zoller, H. Ritsch, *Phys. Rev. A* 45 (1992) 4879.
- [33] R. Dum, A.S. Parkins, P. Zoller, C.W. Gardiner, *Phys. Rev. A* 46 (1992) 4382.
- [34] K. Mølmer, Y. Castin, J. Dalibard, *J. Opt. Soc. Am. B* 10 (1993) 524.
- [35] B. Wolfseder, W. Domcke, *Chem. Phys. Lett.* 259 (1996) 113.
- [36] J. Steinbach, B.M. Garraway, P.L. Knight, *Phys. Rev. A* 51 (1995) 3302.
- [37] B. Wolfseder, Ph.D. Thesis, Technical University of Munich, 1997, unpublished.
- [38] B. Wolfseder, W. Domcke, to be published.
- [39] S. Mukamel, *Principles of Nonlinear Optical Spectroscopy*, University Press, Oxford, 1995.
- [40] W. Domcke, G. Stock, *Adv. Chem. Phys.* 100 (1997) 1.
- [41] L. Seidner, G. Stock, W. Domcke, *J. Chem. Phys.* 103 (1995) 3998.
- [42] B. Wolfseder, L. Seidner, G. Stock, W. Domcke, *Chem. Phys.* 217 (1997) 275.
- [43] W.T. Pollard, R.A. Mathies, *Annu. Rev. Phys. Chem.* 43 (1992) 497.
- [44] G. Stock, W. Domcke, *Chem. Phys.* 124 (1988) 227.
- [45] G. Stock, W. Domcke, *Phys. Rev. A* 45 (1992) 3032.